


RESEARCH ARTICLE

# Mechatronics design of self-adaptive under-actuated climbing robot for pole climbing and ground moving

Yuwang Liu<sup>1,2,\*</sup> , Yi Yu<sup>1,2</sup>, Dongqi Wang<sup>1,2</sup>, Sheng Yang<sup>1,2</sup> and Jinguo Liu<sup>1,2</sup>

<sup>1</sup>State Key Laboratory of Robotics, Shenyang Institute of Automation, Chinese Academy of Sciences, Shenyang, P.R China and

<sup>2</sup>Institutes for Robotics and Intelligent Manufacturing, Chinese Academy of Sciences, Shenyang, P.R China

\*Corresponding author. E-mail: [liuyuwang@sia.cn](mailto:liuyuwang@sia.cn)

**Received:** 31 December 2020; **Revised:** 14 October 2021; **Accepted:** 18 October 2021;

**First published online:** 23 November 2021

**Keywords:** underactuated mechanism, climbing robot, self-adaptive holding, model reference adaptive control, ground moving

## Abstract

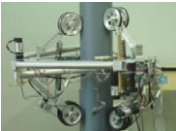

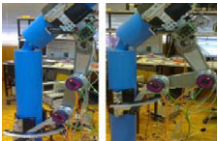
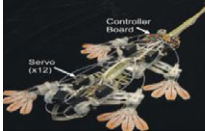
Climbing robots have broad application prospects in aerospace equipment inspection, forest farm monitoring, and pipeline maintenance. Different types of climbing robots in existing research have different advantages. However, the self-adaptability and stability have not been achieved at the same time. In order to realize the self-adaptability of holding and climbing stability, this work proposes a new type of climbing robot under the premise of minimizing the driving source. The robot realizes stable multifinger holding and wheeled movement through two motors. At the same time, the robot has two different working modes, namely pole climbing and ground crawling. The holding adaptability and climbing stability are realized by underactuated holding mechanism and model reference adaptive controller (MRAC). On the basis of model design and parameter analysis, a prototype of the climbing robot is built. Experiments prove that the proposed climbing robot has the ability to stably climb poles of different shapes. The holding and climbing stability, self-adaptability, and climbing and crawling speed of the proposed climbing robot are verified by experiments.

## 1. Introduction

As complex automation systems in a specialized field, climbing robots have a short research history. Several studies have been carried out on climbing robots with different types [1–6] of application scenarios, which mainly can be categorized into hug-type climbing robots, clawed climbing robots, grip-type climbing robots, [7] and surface-attached climbing robots, as shown in Table I.

- (1) Hug-type climbing robots: Typical examples of hug-type climbing robots are the WOODY robot [8] for cylindrical trunk and SnakeRobot, [9] the ring type climbing robot [10] and UT-PCR [11] for pole climbing. Hug-type climbing robots have uniform and fairly firm clamping forces; however, due to hug-type design they normally have poor climbing transition ability and adaptability, and their applications are limited within nonbranching trees and cylindrical objects.
- (2) Clawed climbing robots: Clawed climbing robots are like the RiSE robot [12] and Treebot robot. [13] RiSE is a multilegged robot, which achieves climbing by the coordinating movement of multilegs. Treebot is a biped climbing system, which climbs by alternating its biped legs. Although clawed climbing robots have the advantage of transition between different pole and climbing over obstacles, they can only climb trees with soft textures and their motions are discontinuous due to the characteristics of claw structures.
- (3) Grip-type climbing robots: Grip-type robots have higher degrees of freedom (DOF) and special clamping mechanisms. Grip-type climbing robots include 3DCLIMBER, [14] Shady3D, [15] and other climbing robots. [16–21] Because gripper mechanisms can be separated from objects

**Table I.** Typical climbing robot.

Type	Hug-type	Clawed	Grip-type	Surface attached
Name	UT-PCR <sup>11</sup>	Trebot <sup>13</sup>	3DCLIMBER <sup>14</sup>	Stickbot <sup>23</sup>
Working state				
Contact type	Wheel	multiclawed legs	Gripper mechanism	Bionic adhesive legs
Advantage	Stability Pole climbing	Adaptability Discontinue movement	Multi-DOF Complex control system	All terrain Special surface only
Disadvantage	only			

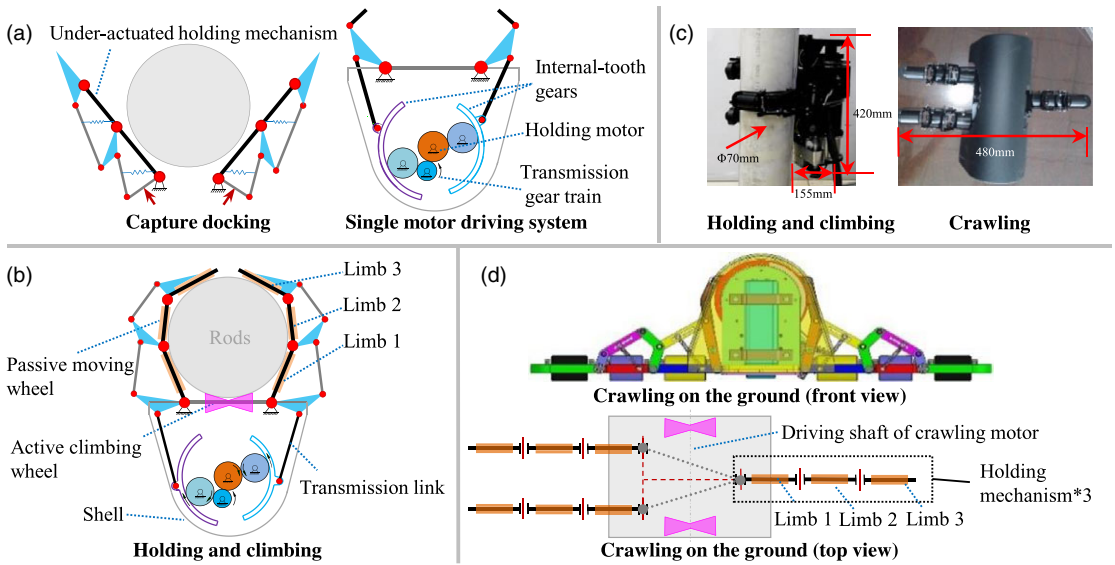
and robot bodies have multi-DOF movements, grip-type climbing robots have strong mobility. However, the multi-DOF characteristic of grip-type climbing robots requires a large number of motors and drives, which enlarge its own weight, reduce the load, and increase the complexity of the controller.

- (4) Surface-attached climbing robots: The representatives of surface-attached climbing robots are the DynaClimber, [22] Stickybot, [23] Gecko-inspired climbing robot. [24–26] DIGbot, and DynaClimber are multifoot robots whose barbs are fixed on the end limbs, and they can climb on mesh and fence. Stickybot is a gecko-bionic robot, which uses villus material on feet with highly efficient symmetrical gait movement mechanism. Magnetic climbing robot could be attached to the metal surface, with a high climbing speed and stability. But application area of these robots is limited, since their movement depends on the characteristics of the climbed surface, and they only climb well on particular surfaces.

The conflicts of current climbing robots mainly include

- (a) The conflict between the demand for multi-action functions and as few drive sources as possible. A large number of drive sources will cause the climbing robot system heavy. However, actual climbing requires the gripper mechanism to have more functions, such as self-adaptability and stability. The requirements of self-adaptability and stability need more drive sources.
- (b) The conflict between the stability, adaptability, and fast movement. An ideal climbing system simultaneously requires the high stability, relatively high adaptability, and high movement efficiency. Existing climbing robots only have one or two of the above characteristics.

The proposed climbing robot is to realize pole climbing and ground crawling with fewer driving sources while ensuring the stability and adaptability of the climbing robot. In this work, a self-adaptive underactuated climbing robot is developed, where an underactuated holding mechanism is designed for stable and self-adaptive holding, and a wheel system is design for climbing and crawling. The underactuated holding mechanism combines the stability of the hug-type climbing robot and the self-adaptive characteristics of the clawed climbing robot. And the underactuated mechanism uses one motor for driving three holding mechanisms, where each of the holding mechanism has three limbs inspired by human-like grasping [27–28]. And an MRAC is designed for stable control of the holding process. Furthermore, integrating the wheel system into the underactuated holding mechanism realizes climbing on the pole and crawling on the ground. Section 2 determines the model design. Section 3 proposes the parameter design. In Section 4, the control design is proposed. The experiments are carried out in Section 5. Finally, conclusions are given in Section 6.



**Figure 1.** Overall schematic design. (a) Underactuated holding mechanism and its driving system. (b) Holding and climbing state diagram. (c) Holding, climbing, and crawling function. (d) Crawling state diagram.

## 2. Model Design

### 2.1. Overview

As shown in Fig. 1, a new type of climbing robot is designed that can realize adaptive grasping, closed envelope clamping, wheel-type locomotion, and crawling on the ground with two drive sources. Based on clamping stability and movement efficiency, as well as the combination of the advantages of high self-adaptability, self-balancing, and high wheeled movement efficiency, a new type of underactuated holding mechanism is developed as shown in Fig. 1(a) and (b). The structure of three limbs simulates human fingers, where one finger has three knuckles. The underactuated holding mechanism compared with two limbs and four limbs is optimal in strength and adaptability. The three holding mechanisms are staggered on the left and right to ensure a wide range of pole holding, and they do not interfere with each other. Moreover, there are two motion modes, which are stably climbing on the pole and crawling on the ground as shown in Fig. 1(c) and (d).

### 2.2. Underactuated holding mechanism

The robot mainly consists of a shell, a base, three underactuated holding mechanisms, a driving system of the holding mechanism, and a wheel driving system, along with the power supply and circuit boards and other related components as shown in Fig. 2. And a total of two motors is applied, where one motor drives the wheel driving system and the other motor drives three holding mechanisms.

The proposed underactuated holding mechanisms drive by one motor, and the three holding mechanisms on both sides of the robot squeeze toward the holding center to realize the circumferential holding of cylindrical objects. Three holding mechanisms synchronously close or open to achieve the adhesion and separation from the climbing object.

The underactuated holding mechanism consists of linkage mechanisms, passive wheels, auxiliary springs, mechanical limits, and related sensors, as shown in Fig. 2. The linkage mechanisms mainly consist of limb 1, limb 2, limb 3, the auxiliary linkage, and three passive wheels arrange on limbs. The springs are located between the limbs and the auxiliary linkages providing auxiliary power for stable opening and closing.

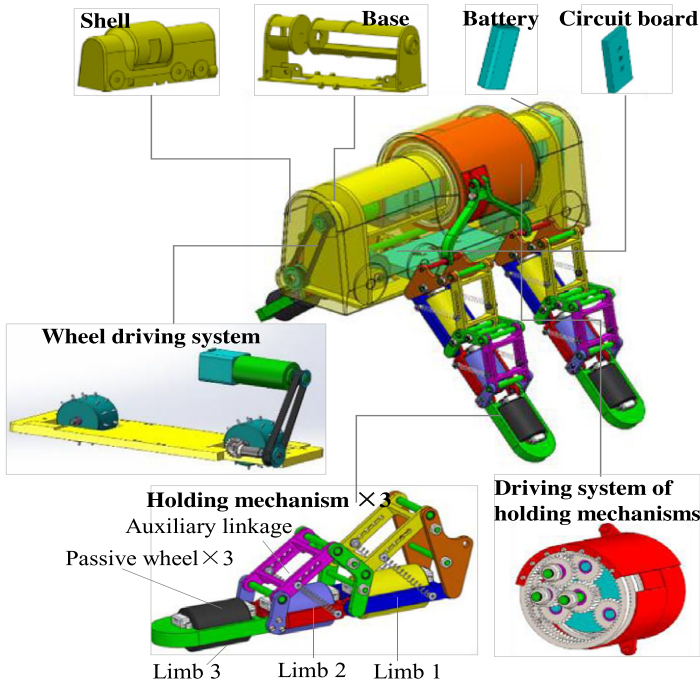


Figure 2. Overall robot model design.

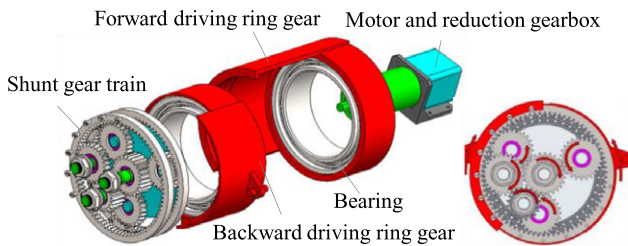


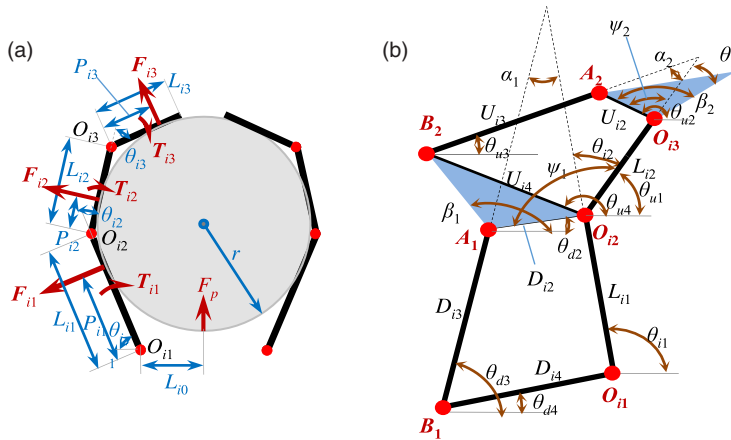
Figure 3. Model of driving system of holding mechanism.

2.3. Driving system of holding mechanisms

Three underactuated holding mechanisms share one drive system. As shown in Fig. 3, the system is mainly composed of a drive motor and a reduction gearbox, a shunt gear train, a forward driver ring gear, a backward driver ring gear, and a bearing. The motor power transfers to the holding mechanisms through a shunt gear train, where two holding mechanisms of right side driven by the forward driving ring gear, one holding mechanism of left side driven by backward driving ring gear. The motor drives the holding mechanisms on both sides of the robot, where each side moves in the opposite direction achieving the holding and releasing functions.

2.4. Wheel driving system

Compared with the climbing robot of clawed, grip-type, and surface-attached type, the wheel driving system is obviously efficient from speed and stability. As shown in Fig. 2, the wheel driving system includes a motor, a belt-driving system, a driving shaft, a gear reversing system, and climbing wheel. Two driving wheels are placed at the front and back of the center line of the base driven by one motor. The design can be integrated effectively with multiple holding mechanisms in a limited space. To ensure the effectiveness and stability, the climbing wheel is equipped with a large number of external round thorns.



**Figure 4.** Mechanical analysis of holding mechanism. (a) Force diagram. (b) Principle of holding mechanism.

### 3. Parameter Design

The parameter design mainly contains two parts: linkage parameters and driving parameters. The under-actuated holding mechanism is the key part of the proposed climbing robot, and its linkage parameters are determined by the size of the holding target. The length of the linkage is optimized by minimizing the difference of contact force of the three limbs. The holding mechanisms realize stable attachment and holding via the motor driving, so the driving force is an important parameter for motor selection.

#### 3.1. Link parameter determination of the holding mechanism

The holding mechanism is an underactuated multilink mechanism, including two parts, three limbs and auxiliary links. The length parameters of the three limbs are set relative to the forces condition of the holding mechanism. In addition to being associated with the force condition, the length parameters of the auxiliary links are associated with the link kinematics.

##### 3.1.1. Force and transmission ratio analysis of limbs.

The contact force of each limb at the contact point directly affects climbing stability and reliability and is an important constraint in parameter optimization design [29]. The overall force is shown in Fig. 4(a), when all limbs of three holding mechanisms on both sides of the robot are contacted with the pole. The weight of all joints and the friction between kinematic pairs are neglected in force analysis.

The transmission ratio  $R_{ij}$  of  $i$ th holding mechanism is defined as the ratio of adjacent driving torque of the limbs; thus,

$$R_{ij} = \frac{T_{i(j+1)}}{T_{ij}} \quad (i = 1, 2, 3; j = 1, 2) \tag{1}$$

In Eq. (1), there are two ratios  $R_{i1}$  and  $R_{i2}$  between three limbs of  $i$ th holding mechanism, and the ratios vary with the rotation of the limb. By the geometric relationship in Fig. 4(a), it can be obtained

$$R_{i2} = \frac{(L_{i2} + P_{i1} - L_{i1}) (r^2 + (L_{i2} + P_{i1} - L_{i1})^2)}{(2L_{i2} + P_{i1} - L_{i1}) r^2 + (L_{i2} + P_{i1} - L_{i1})^2 (P_{i1} - L_{i1})} \tag{2}$$

$$R_{i1} = \frac{(L_{i1} - P_{i1}) (L_{i2} + P_{i1} - L_{i1}) (r^2 + (L_{i1} - P_{i1})^2) (r^2 + (L_{i2} + P_{i1} - L_{i1})^2)}{M + N - K + J - Q} \tag{3}$$

Table II. Nomenclature.

Symbol	Definition
$O_{ij}$	Rotation axis of the $j$ limb of holding mechanism $i$ ( $i = 1,2,3; j = 1,2,3$ )
$F_{ij}$	Contact force with object of the $j$ limb of holding mechanism $i$ ( $i = 1,2,3, j = 1,2,3$ )
$L_{ij}$	Length of the $j$ limb of holding mechanism $i$ ( $i = 1,2,3, j = 1,2,3$ )
$L_{i0}$	Distance between holding mechanism $i$ and centerlines of the base ( $i = 1,2,3$ )
$P_{ij}$	Distance between $O_{ij}$ and the contact point, which is the $j$ limb of holding mechanism $i$ with object ( $i = 1,2,3, j = 1,2,3$ )
$T_{ij}$	Driving torque of the $j$ limb of holding mechanism $i$ ( $i = 1,2,3, j = 1,2,3$ )
$\theta_{ij}$	Turning angle of $j$ limb of holding mechanism $i$ relative to the $(j-1)$ limb ( $i = 1,2,3, j = 1,2,3, j = 1$ represents the turning angle relative to the base)
$R_{ij}$	Transmission ratio of the holding mechanism (driving torque ratio of two adjacent limbs)
$r$	Radius of the object climbed by the robot
$r0$	Radius of drive crawling wheel
$D_{ij}$	Length of each link in the lower four-bar linkage of holding mechanism $i$ ( $j = 2,3,4$ ), $D_{i2}$ , $D_{i3}$ and $D_{i4}$ , respectively, represent the length of upper, left and down link in the lower four-bar linkage in Fig. 2(b) (right link is limb link, and its length is $L_{i1}$ )
$U_{ij}$	Length of each link in upper four-bar linkage of holding mechanism $i$ ( $j = 2,3,4$ ), $U_{i2}$ , $U_{i3}$ , and $U_{i4}$ represent the length of upper, left and down link in the lower four-bar linkage in Fig. 2(b), respectively (right link is limb link, and its length is $L_{i2}$ )
$\theta_{dj}$	Angle between each link in lower four-bar linkage and horizontal line ( $j = 2,3,4$ ), $\theta_{d2}$ , $\theta_{d3}$ , and $\theta_{d4}$ , respectively, represent the angles of upper, left, and down links in lower four-bar linkage with the horizontal line in Fig. 2(b)
$\theta_{uj}$	Angle between each link in upper four-bar linkages and horizontal line ( $j = 2,3,4$ ), $\theta_{u2}$ , $\theta_{u3}$ , and $\theta_{u4}$ , respectively represent the angle of upper, left and down links in upper four-bar linkage with the horizontal line in Fig. 2(b)
$\Psi_j$	$j = 1,2$ , $\Psi_1$ and $\Psi_2$ , respectively, represent the top link structural angle between the lower and upper four-bar linkages (Fig. 2(b))
$\mu_0$	Friction coefficient between the driven wheel of holding mechanism and object
$\mu_1$	Friction coefficient between the crawling drive wheel and the object
$Mg$	Gravity acting on the entire crawling robot
$T_{id}$	Input torque of the drive gear ring of holding mechanism $i$
$T_{a1}$	Output torque of the holding mechanism's drive motor through reducer amplified
$T_{a2}$	Driving torque of the drive wheel's motor through reducer amplified
$Z_1$	Teeth of main drive gear
$Z_3$	Teeth of drive ring gear
$q$	Diameter on graduated circle of drive ring
$\gamma$	Angle between the connection of the head joint node with casing center and frame in the horizontal direction
$h$	Torque ratio of the output link and input link in four-bar linkage

where

$$\begin{cases}
 M = (1 - R_{i2}) (L_{i1} - P_{i1}) (L_{i2} + P_{i1} - L_{i1}) (r^2 + (L_{i1} - P_{i1})^2) (r^2 + (L_{i2} + P_{i1} - L_{i1})^2) \\
 N = L_{i1} (L_{i2} + P_{i1} - L_{i1}) (r^2 - (L_{i1} - P_{i1})^2) (r^2 + (L_{i2} + P_{i1} - L_{i1})^2) \\
 K = R_{i2} L_{i1} (L_{i1} - P_{i1}) (r^2 - (L_{i1} - P_{i1})^2) (r^2 - (L_{i2} + P_{i1} - L_{i1})^2) \\
 J = 4R_{i2} L_{i1} r^2 (L_{i1} - P_{i1}) (L_{i2} + P_{i1} - L_{i1}) \\
 Q = R_{i2} L_{i2} (L_{i1} - P_{i1}) (r^2 + (L_{i1} - P_{i1})^2) (r^2 - (L_{i2} + P_{i1} - L_{i1})^2)
 \end{cases} \tag{4}$$

By Eq. (2), the transmission ratio  $R_{i2}$  between limb 3 and limb 2 of the  $i$  holding mechanism is related to parameters  $L_{i0}$ ,  $L_{i1}$ ,  $L_{i2}$ ,  $P_{i1}$ , and  $r$ .  $R_{i2}$  variation with changes of  $L_{i1}$ ,  $L_{i2}$ ,  $r$  is shown in Fig. 4(a). In order

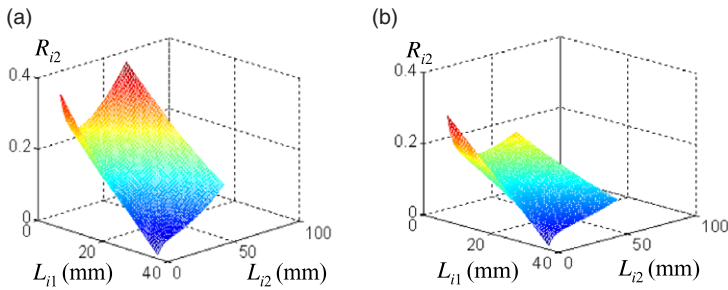


Figure 5. Transmission ratio  $R_{i2}$  changing with  $L_{i1}$  and  $L_{i2}$ . (a)  $r = 35$  mm. (b)  $r = 60$  mm.

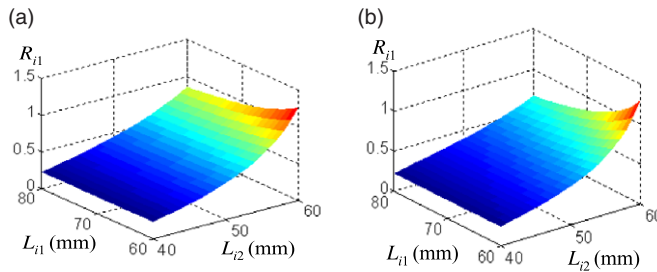


Figure 6. Transmission ratio  $R_{i1}$  changing with  $L_{i1}$  and  $L_{i2}$ . (a)  $r = 35$  mm,  $R_{i2} = 0.4$ . (b)  $r = 55$  mm,  $R_{i2} = 0.5$ .

to achieve 40–100 mm pole climbing, the middle value of the target range for calculation is selected. When given  $r = 70$  mm, it means  $L_{i0} = 20$  mm and  $P_{i1} = 30$  mm, as shown in Fig. 5. So  $R_{i2}$  decreases when  $r$  increases, the maximum value of  $R_{i2}$  is no more than 0.5, that is,  $R_{2max} \leq 0.5$ . By Eq. (3), the transmission ratio  $R_{i1}$  between limb 2 and limb 1 of  $i$ th holding mechanism is related to  $L_{i0}$ ,  $L_{i1}$ ,  $L_{i2}$ ,  $P_{i1}$ ,  $r$ , and  $R_{i2}$ .

When given  $L_{i0} = 20$  mm and  $P_{i1} = 30$  mm, the variation of  $R_{i1}$  with changes of  $L_{i1}$ ,  $L_{i2}$ ,  $r$ , and  $R_{i2}$  is shown in Fig. 6. As it can be seen,  $R_{i1}$  decreases with the increase of  $r$ , but the maximum value of  $R_{i1}$  is no more than 1, that is,  $R_{1max} \leq 1$ .

### 3.1.2 Kinematic analysis of holding mechanism.

The holding mechanism can be seen as consisting of two four-link subsystems in series, and its geometric model diagram is shown in Fig. 4(b). In Eq. (1), the transmission ratio  $R$  of the limbs of the holding mechanism can be rederived from the linkage mechanism, as shown in Table III. The transmission ratios  $R_{i1}$  and  $R_{i2}$  are related to the four-link design parameters, where  $R_{i1}$  is the function of the lower part of the four-link mechanism parameters  $L_{i1}$ ,  $D_{i2}$ ,  $D_{i3}$ ,  $D_{i4}$ ,  $\beta_1$  and rotation angle  $\theta_{i2}$ ;  $R_{i2}$  is a function of the upper part of the four-link mechanism parameters  $L_{i1}$ ,  $U_{i2}$ ,  $U_{i3}$ ,  $U_{i4}$ ,  $\beta_2$  and rotation angle  $\theta_{i3}$ .

### 3.1.3 Parameter optimization of the holding mechanism:

As all limbs of the holding mechanism contact with the pole and the contact forces of each holding mechanism are assumed to be equal, the robot can stably hold the object. However, in fact the contact forces of the three limbs of each holding mechanism will have differences. As the minimum differences of contact force among three limbs is the optimization target, the optimization function for  $i$ th holding mechanism is established:

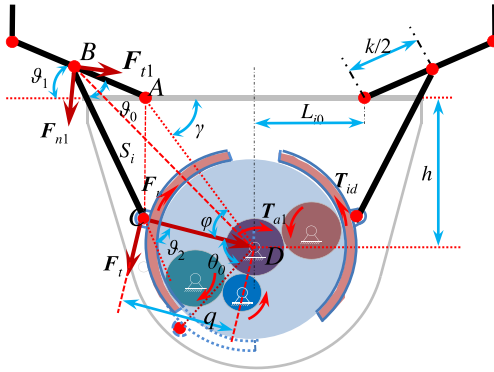


Figure 7. Transmission system sketch.

$$\min f(\mathbf{X}) = \min \left( \sum_{n=1}^3 (F_{in} - F_{i3})^2 + \sum_{n=1}^2 (F_{in} - F_{i2})^2 \right)$$

$$\mathbf{x} = [L_{i1} \ D_{i2} \ D_{i3} \ D_{i4} \ \beta_1 \ L_{i2} \ U_{i2} \ U_{i3} \ U_{i4} \ \beta_2]^T \tag{5}$$

where

$$\begin{cases} F_{i1} = \frac{T_{i1}}{P_{i1}} \left( 1 - R_{i1} \left( \frac{P_{i2} + L_{i1} \cos \theta_{i2}}{P_{i2}} - \frac{R_{i2}}{P_{i3}} (P_{i3} + L_{i2} \cos \theta_{i3} + L_{i1} \cos (\theta_{i2} + \theta_{i3})) \right) \right) \\ F_{i2} = \frac{T_{i1} R_{i1}}{P_{i2}} \left( 1 - \frac{R_{i2}}{P_{i3}} (P_{i3} + L_{i2} \sin \theta_{i3}) \right); F_{i3} = \frac{T_{i1} R_{i1} R_{i2}}{P_{i3}} \end{cases} \tag{6}$$

Above constraints mainly include the transmission ratio constraint and the link transmission angle constraint. The constraint functions of transmission ratios are derived in Figs. 3, 4 and Table III, and the constraint functions of the transmission angle are derived by the link transmission principle and Fig. 4(b). The results are shown in Table IV.

According to the actual situation, the initial values are given, the link parameters of the ultimate holding mechanism are determined finally based on the established optimization function and constraints, as shown in Table V.

### 3.2. Parameter calculation of the drive system

The whole robot has two motors, that is, the holding motor for three holding mechanisms and the driving motor for the wheel system, respectively. The required values of driving forces and critical parameters of the transmission system for two motors are computed below.

#### 3.2.1. Driving torque calculation of the holding mechanism.

The drive system schematic of the holding mechanisms is shown in Fig. 7.

By the vector equation and the horizontal axis projection, we have

$$0.5k \cos \vartheta_1 - S_i \cos (\vartheta_0 + \vartheta_1) = q \cos (\vartheta_0 + \vartheta_1 - \vartheta_2) - \sqrt{L_{i0}^2 + h^2} \cos \gamma \tag{7}$$

In Eq. (7), the parameter  $k$  can be obtained by parameters of  $F_{in}$  ( $n = 1, 2, 3$ ) in Tables III and V.  $L_{i0}$ ,  $S_i$ ,  $\gamma$ , and  $h$  are the structural parameters, which can be determined from Fig. 7 and Table V.  $q$ ,  $Z_1$ ,  $k$ , and  $Z_3$  are design parameters, and the given values are shown in Table VI.  $\vartheta_0$ ,  $\vartheta_1$ ,  $\vartheta_2$ , and  $\varphi$  are design variables.

In the critical state of climbing on vertical cylindrical objects, the sum of friction between the robotic limbs and the climbed object equals the gravity of the robot. Assuming that each limb is in contact with



**Table III.** Transmission ratios of the multilinkage holding mechanism.

Upper four-bar mechanism	Lower four-bar mechanism
$R_{i1} = \frac{h_1}{h_1 + L_{i1}}$	$R_{i2} = \frac{h_2}{h_2 + L_{i2}}$
$h_1 = D_{i2} (\cos (\theta_{i2} - \psi_1) - \sin (\theta_{i2} - \psi_1) \cot \alpha_1)$	$h_2 = U_{i2} (\cos (\theta_{i3} - \psi_2) - \sin (\theta_{i3} - \psi_2) \cot \alpha_2)$
$\cot \alpha_1 = \frac{D_{i2} \sin (\theta_{i2} - \psi_1) \sqrt{4 D_{i4}^2 D_{i3}^2 - N_1^2} + M_1 (L_{i1} + D_{i2} \cos (\theta_{i2} - \psi_1))}{-(L_{i1} + D_{i2} \cos (\theta_{i2} - \psi_1)) \sqrt{4 D_{i4}^2 D_{i3}^2 - N_1^2} + M_1 D_{i2} \sin (\theta_{i2} - \psi_1)}$	$\cot \alpha_2 = \frac{U_{i2} \sin (\theta_{i3} - \psi_2) \sqrt{4 U_{i4}^2 U_{i3}^2 - N_2^2} + M_2 (L_{i2} + U_{i2} \cos (\theta_{i3} - \psi_2))}{-(U_{i2} + U_{i3} \cos (\theta_{i3} - \psi_2)) \sqrt{4 U_{i4}^2 U_{i3}^2 - N_2^2} + M_2 U_{i2} \sin (\theta_{i3} - \psi_2)}$
$M_1 = -L_{i1} (L_{i1} + 2 D_{i2} \cos (\theta_{i2} - \psi_1)) + D_{i3}^2 - D_{i4}^2 - D_{i2}^2$	$M_2 = -L_{i2} (L_{i2} + 2 U_{i2} \cos (\theta_{i3} - \psi_2)) + U_{i4}^2 - U_{i3}^2 - U_{i2}^2$
$N_1 = L_{i1} (L_{i1} + 2 D_{i2} \cos (\theta_{i2} - \psi_1)) - D_{i4}^2 - D_{i3}^2 + D_{i2}^2$	$N_2 = L_{i2} (L_{i2} + 2 U_{i2} \cos (\theta_{i3} - \psi_2)) - U_{i4}^2 - U_{i3}^2 + U_{i2}^2$

**Table IV.** Constraints of optimization functions.

Transmission angle constraint of lower four bar	$\frac{D_{i3}^2 + D_{i2}^2 - D_{i4}^2 - L_{i1}^2}{2D_{i3}D_{i2}} > \cos 135^\circ$
	$\frac{D_{i3}^2 + D_{i2}^2 - D_{i4}^2 - L_{i1}^2 + 2D_{i4}L_{i1}\cos\theta_{d4}}{2D_{i3}D_{i2}} < \cos 45^\circ$
Transmission angle constraint of upper four bar	$\frac{U_{i3}^2 + U_{i2}^2 - U_{i4}^2 - L_{i2}^2}{2L_{i2}U_{i2}} > \cos 135^\circ$
	$\frac{U_{i3}^2 + U_{i2}^2 - U_{i4}^2 - L_{i2}^2 + 2U_{i3}L_{i2}\cos\theta_{21}}{2L_{i2}U_{i2}} < \cos 45^\circ$
Constraint of $R_{i1}$	$0 < \frac{D_{i2}\cos(\theta_{i2} - \psi_1) - \sin(\theta_{i2} - \psi_1)\cot\alpha_1}{D_{i2}\cos(\theta_{i2} - \psi_1) - \sin(\theta_{i2} - \psi_1)\cot\alpha_1 + L_{i1}} < 1$
Constraint of $R_{i2}$	$0 < \frac{U_{i2}\cos(\theta_{i3} - \psi_2) - \sin(\theta_{i3} - \psi_2)\cot\alpha_2}{U_{i2}\cos(\theta_{i3} - \psi_2) - \sin(\theta_{i3} - \psi_2)\cot\alpha_2 + L_{i2}} \leq 0.5$

**Table V.** Parameter optimization results of holding links.

Upperfour-bar	The initial giving value (mm)			
	$L_{i1}$	$U_{i2}$	$U_{i3}$	$U_{i4}$
	45	14	34	24
	The final optimized value (mm)			
	$L_{i1}$	$U_{i2}$	$U_{i3}$	$U_{i4}$
	45	12	32.6264	26
Lowerfour-bar	The initial giving value (mm)			
	$L_{i2}$	$D_{i2}$	$D_{i3}$	$D_{i4}$
	35	15	47	32
	The final optimized value (mm)			
	$L_{i2}$	$D_{i2}$	$D_{i3}$	$D_{i4}$
	35	10	40.001	31.998

**Table VI.** Given parameter values.

$q$ (mm)	$Z_1$	$k$ (mm)	$Z_3$
100	20	57.5	80
$S_i$ (mm)	$L_{i0}$ (mm)	$\gamma$	$h$ (mm)
82	45	60	86

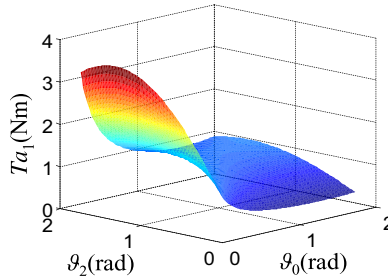
the object, and the contact forces are equal (three unequal contact forces  $F_{ij}$  are regard as three equal contact forces  $f$ ), it can be inferred that

$$\sum_{i=1}^3 (F_{i1} + F_{i2} + F_{i3}) = 9f \tag{8}$$

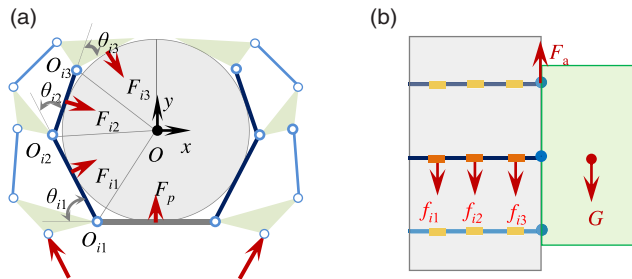
And the relationship between friction and gravity can be described as follow:

$$9\mu f = Mg \tag{9}$$

When the diameter of holding pole is 70 mm, and the robotic mass is 3.5 kg, and the coefficient of friction  $\mu$  between the limbs and the object is 0.3, it can be inferred that  $f = Mg / (9\mu) = 12.96N$ . Under the assumption of neglecting friction and spring forces, the contact force of the contact points is[22]



**Figure 8.** Change condition for the driving torque of the holding mechanism, varying with push shaft posture.



**Figure 9.** Force diagrams in the climbing process. (a) Plan view. (b) Front view.

$$\mathbf{f} = \begin{bmatrix} \frac{P_{i2}(1 + R_1) + R_1 L_{i1} \cos \theta_{i2}}{P_{i1} P_{i2}} T_{i1} \\ -\frac{R_1}{P_{i2}} T_{i1} \end{bmatrix} = \begin{bmatrix} 12.96 \\ 12.96 \end{bmatrix} \tag{10}$$

where  $R_1 = 0.19$  and  $\cos \theta_{i2} = 0.6$ . By Eq. (10), it can be found that  $T_{i1} = f \cdot P_{i2} / R_1 = 1.36 \text{ N} \cdot \text{m}$ , and it can be obtained,

$$T_{a1} = \frac{qZ_1 \sin \vartheta_2 T_{i1}}{kZ_3 \sin \vartheta_0} = \frac{0.592 \sin \vartheta_2}{\sin \vartheta_0} \tag{11}$$

By Eq. (11), the driving torque varies with the changes of attitude angle  $\vartheta_0$  and  $\vartheta_2$  of driving push shaft, and the trend is shown in Fig. 8. From Fig. 8, when limb 3 is in contact with the pole, the drive torque reaches the maximum value to 3.2 N·m, where  $\vartheta_0 = 16^\circ$ ,  $\vartheta_2 = 80^\circ$ . When all the holding mechanisms are in contact with the pole, the driving torque of the robot will maintain a fixed value.

### 3.2.2 Climbing driving torque calculation.

The overall stress schematic for climbing process is shown in Fig. 9.

By Newton’s second law and force equilibrium conditions, the minimum output torque of climbing wheels is obtained

$$T_{a2\min} = 3F_{i1} \mu_0 r_0 \begin{pmatrix} 3 + \cos \theta_{i1} - \cos (\theta_{i1} + \theta_{i2}) \\ -\cos (\theta_{i1} + \theta_{i2} + \theta_{i3}) \end{pmatrix} \tag{12}$$

When the parameter values shown in Table VII are given, the relation for torque variation with the parameters is shown in Fig. 10, respectively.

Table VII. Given parameter values.

$\mu_0 = \mu_1$	$r_0$ (mm)	$F_{i1} = F_{i2} = F_{i3}$ (N)	$\theta_{i1}, \theta_{i2}, \theta_{i3}$ (rad)
0.25	25	5~120	0 ~ $\Pi/2$

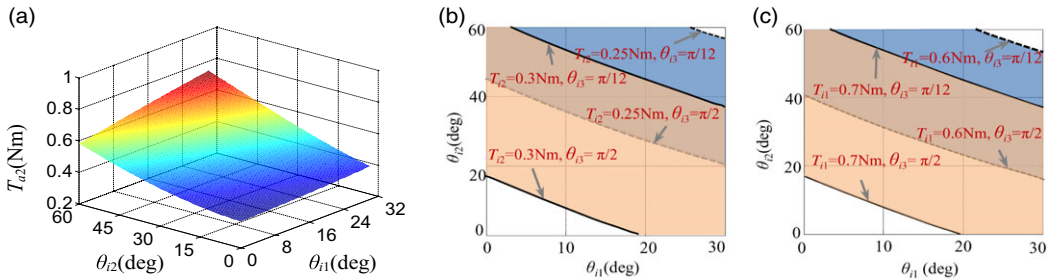


Figure 10.  $T_{a2}$  changes with variable  $\theta_{i1}, \theta_{i2}, F_{i1}, \theta_{i3}$ . (a) When  $F_{i1} = 120$  N,  $T_{a2}$  changes with  $\theta_{i1}, \theta_{i2}$ . (b) When  $F_{i1} = 5$  N,  $T_{12}$  changes with  $\theta_{i1}, \theta_{i2}$ . (c) When  $F_{i1} = 120$  N,  $T_{11}$  changes with  $\theta_{i1}, \theta_{i2}$ .

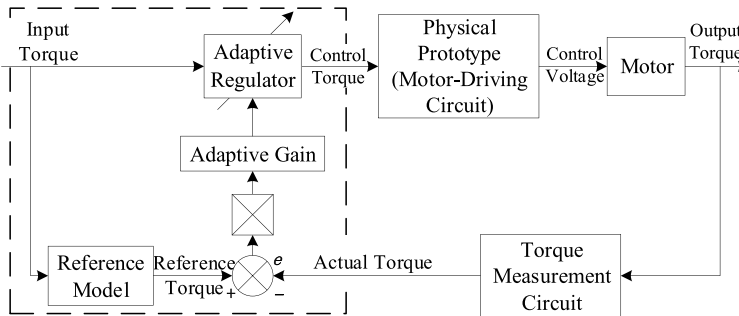


Figure 11. Control system model.

4. Control Design

The control system model of the climbing robot is shown in Fig. 11. The hardware of the system is composed by a control circuit, a motor-driving circuit, and a torque measurement circuit. MRAC controller is within the dashed box. The system configuration uses STM32F405RGT6. The chip is a powerful member of the STM32 family with enhanced DSP processing instructions, clocked at 168 MHz (210DMIPS), with powerful hardware floating-point computing power, up to 1M bytes of on-chip memory, and 196K bytes of embedded SRAM. The chip uses Thumb-2 instruction system with a single-cycle 32-bit hardware multiply unit and a 16-bit SIMD calculation unit. The algorithm relies on the embedded real-time operating system  $\mu C/OSII$ .

First, error between reference torque and actual torque transfers from adaptive gain to adaptive regulator. Second, adaptive regulator integrates input torque and adaptive gain to calculate the control torque. Finally, holding mechanism is driven to action response.

The multilink mechanisms and the springs have the characteristic of rigid-flexible coupling, which provide a certain degree of adaptability itself. In order to better exert the adaptive advantages of holding mechanism, MRAC with adjustable gain is designed. Therefore, the robot moves along the desired trajectory  $u_d(t)$  and tends to asymptotic stability. The system structure of proposed Lyapunov-MRAC controller is shown in Fig. 12, where the physical quantities are given in Table VIII.  $A_m$  and  $A_p$  are system matrixes, and  $B_m$  and  $B_p$  are input matrixes.  $C_m$  and  $C_p$  are matrixes combining centrifugal force.  $x_m$  and  $x_p$  are vectors obtained by  $\theta_{ij}$ . The error between the object model and the reference model adjusts the controller gain  $k_a(t)$  via the coefficient  $k_g$  as shown in Fig. 12. Then, the object model is compensated

Table VIII. Parameters of input and output.

Input and output	Actual meaning	Physical meaning
Reference input $u_d(t)$	Desired drive torque of motor	Torque
Controller input $u(t)$	Input for controller after feedback signal	Torque
Model output $y_m(t)$	Derived output of dynamics model	Torque
Object output $y_p(t)$	Actually collected output of motor	Torque

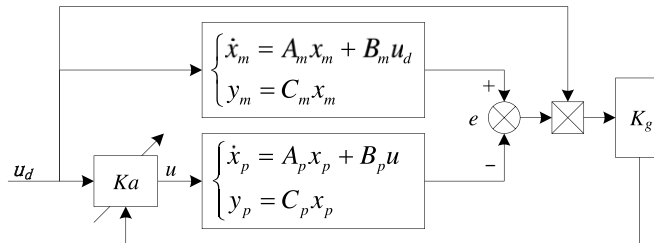


Figure 12. Block diagram of Lyapunov-MRAC controller system.

by  $k_a(t)$ .

$$u(t) = k_a(t) u_d(t) \tag{13}$$

The design task of the controller is to seek the regulation law of the adjustable controller gain  $k_a(t)$  according to the Lyapunov stability theory, so that  $e$  tends to zero. The gain difference  $k$  and the error  $e(t)$  are expressed as

$$\begin{cases} e(t) = y_m(t) - k_a(t) y_p(t) = k \frac{Y(p)}{U(p)} u_d(t) \\ k = k_m - k_a(t) k_p \end{cases} \tag{14}$$

Equation (14) converts into an observable canonical form of the state space,

$$\begin{cases} \dot{x} = Ax + kBu_d \\ e = Cx \end{cases} \tag{15}$$

The Lyapunov function is defined as  $V = k_v x^T Px + k^2$ , where  $k_v > 0$ , then,

$$\dot{V} = -k_v x^T Qx + 2k(\dot{k} + k_v u_d B^T Px) \tag{16}$$

$k_p$  slowly changes with time and can be approximated as a constant.  $k_m$  is a constant. In order to make  $\dot{V} < 0$ , by Eq. (16), the parameter adaptive regulation law is

$$\begin{cases} \dot{k} = -k_v u_d B^T Px \\ \dot{k}_a \approx -\frac{\dot{k}}{k_p} = \frac{k_v}{k_p} u_d B^T Px \end{cases} \tag{17}$$

By Eqs. (15) and (17), the model of the adjustable gain refers to the adaptive control law which is as follows:

$$\dot{k}_a(t) = k_g u_d(t) e(t) \tag{18}$$

where  $k_g$  is the adaptive gain, and  $k_g > 0$ .

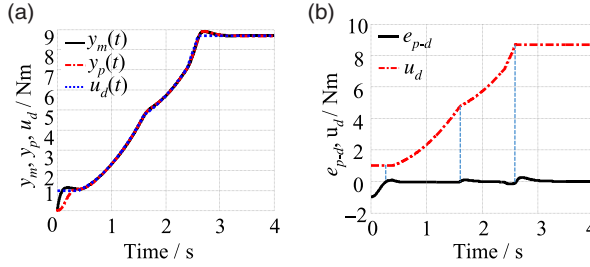


Figure 13. Control performance and fluctuation curve of error.

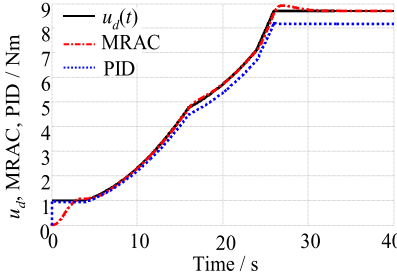


Figure 14. Response curve of MRAC algorithm and traditional PID.

The above proposed model is simulated in MATLAB, taking an adaptive gain  $k_g = 1.1$ , and Coriolis forces are as shown in Eq. (19).

$$A = \begin{bmatrix} 0 & 0 & 0 & 1 & 0 & 0 \\ 0 & 0 & 0 & 0 & 1 & 0 \\ 0 & 0 & 0 & 0 & 0 & 1 \\ 0 & 5.4 & 3.7 & 0 & 0 & 0 \\ 0 & -19.1 & 19.2 & 0 & 0 & 0 \\ 0 & 19.2 & -60.6 & 0 & 0 & 0 \end{bmatrix}, \quad B = \begin{bmatrix} 0 \\ 0 \\ 0 \\ 1 \\ -1.1 \\ -0.8 \end{bmatrix}, \quad C = \begin{bmatrix} 1.3 \\ 2.7 \\ 1.1 \\ 2.1 \\ 1.9 \\ 1.3 \end{bmatrix} \quad (19)$$

The simulation results are shown in Fig. 13(a). Contrasting  $u_d(t)$  and  $y_m(t)$ , there are hysteresis at initial interval and overshoot at the end interval due to the inertia unit in holding mechanism. Contrasting  $u_d(t)$  and  $y_p(t)$ , the control system can drive the robot well and complete the holding task. As shown in Fig. 13(b) is the error curve ( $e_{p-d}$ ) between actual output  $y_p(t)$  and given input  $u_d(t)$ . Large change rate of the drive torque results in large errors at the beginning of each stage when three limbs of each holding mechanism contact with target object in turn. But the errors tend to 0 by the controller adjusting.

The response curves of the designed MRAC controller and the traditional PID controller are compared as shown in Fig. 15. After many rounds of debugging, the optimal PID parameters  $K_p = 25$ ,  $K_i = 1.1$ , and  $K_d = 1.7$  are obtained. The output response of the PID controller is well preformed at 0~9 s in Fig. 14, but the steady-state error is getting larger and larger at later stage. The designed Lyapunov-MRAC controller achieves a good follow-up to the desired curve after 3 s with a small steady-state error, which means that the controller realizes the stability of the underactuated holding mechanisms.

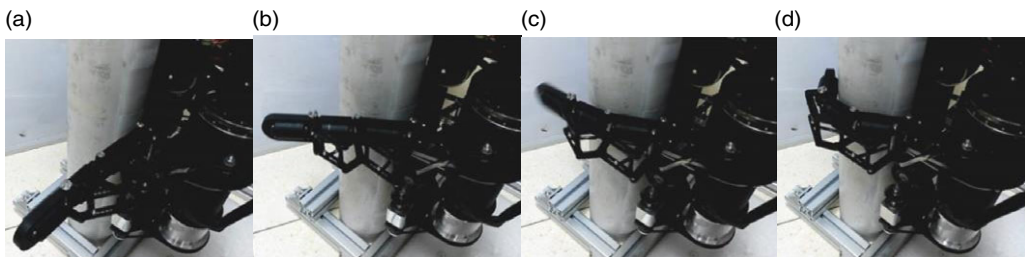
## 5. Experiment of the Prototype

### 5.1. Prototype establishment

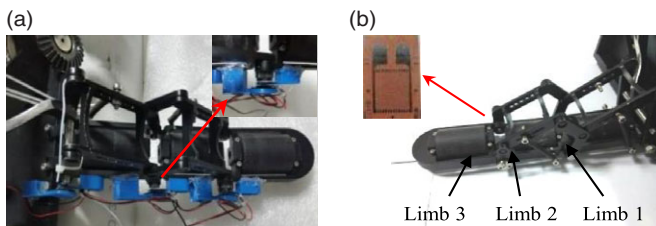
According to the parameter design, the key given parameters are shown in Table IX. A physical prototype of the underactuated climbing robot with the length of 420 mm, width of 480 mm, and height of about

**Table IX.** Key parameters of climbing robot.

Parameters	Value
Distance between the left and right sides of the holding mechanism	90 mm
Distance between the two holding mechanisms of the right side	110 mm
Front and back length of the robot (base length)	420 mm
Base height of the robot	145.5 mm
The maximum outer diameter of the driving circle of holding mechanism	48 mm
Length of limb 1	65 mm
Length of limb 2	55 mm
Length of limb 3	70 mm
Passive wheel diameter	30 mm
Driving wheel diameter	42~50 mm
Holding nominal torque	4.26 N·m



**Figure 15.** Whole process of holding movement. (a) Target object. (b) First limb contacting with target object. (c) Second limb contacting with target object. (d) Third limb contacting with target object.



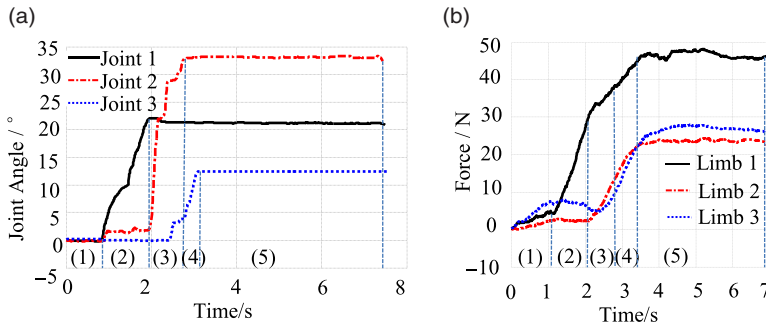
**Figure 16.** Experimental measurement platform of the pole-climbing robot. (a) Measuring device of joint angle. (b) Measuring device of contact force.

155 mm is built. The drive shaft is made of No. 45 steel, the supporting parts are made of aluminum alloy, and the nonsupporting parts are made of polyester plastic and processed by 3D printing to reduce the weight of the climbing robot. Total weight of the climbing robot is 5.9 kg.

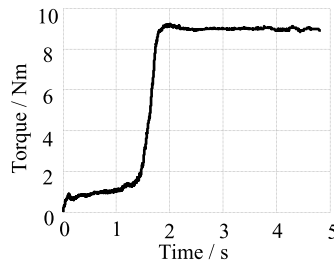
**5.2. Underactuated holding experiment**

The holding process of the climbing robot is implemented and shown in Fig. 15. The experiment results are carried out for physical prototype verification. The 50 kΩ potentiometers with 1% precision are used to measure the angle changes of each joint, as shown in Fig. 16(a). The potentiometers are placed on the outside of the limb, collinear with the joint axis. The contact forces of each limb are measured by the metal strain gauges, with values of 350 Ω and sensitivity of 2.0, as shown in Fig. 16(b).

Multiple repeated experiments are made on the constructed platform. The experimental data are transmitted to PC through a serial communication device. The response curves of the joint angles and the contact forces are shown in Fig. 17. As it can be seen from Fig. 17, the joint angles are 12.2°, 33.8°,



**Figure 17.** Response curve of joint angle and contact force. (a) Response curve of joint angular. (b) Response curve of contact force.



**Figure 18.** Output torque response curve of holding motor.

and  $21.5^\circ$ , followed by the contact force are 48, 20, and 28 N. From the change curve of the joint angles and the contact forces, the holding process of the robot can be subdivided into five stages, namely (1) not contact with target object, (2) the first limb contacting target object, (3) the second limb contacting target object, (4) the third limb contacting target object, and (5) motor continuing working to reach the required climbing friction. Design decision optimizes structure of robot, so that robot can hold and climb more steadily. The final contact forces of limbs are mostly smooth, and holding process is stable and reliable. This proves that the robot with the underactuated mechanism has good holding stability.

In Fig. 18, the output torque of the holding motor is obtained by measuring the motor output in real-time. The total holding time is 4.7 s, the holding torque is 9.1 N·m, the overshoot is 0.5 N·m, and the steady state error is 0.13 N·m. The designed adjustable gain Lyapunov-MRAC controller is stable with a low steady-state error.

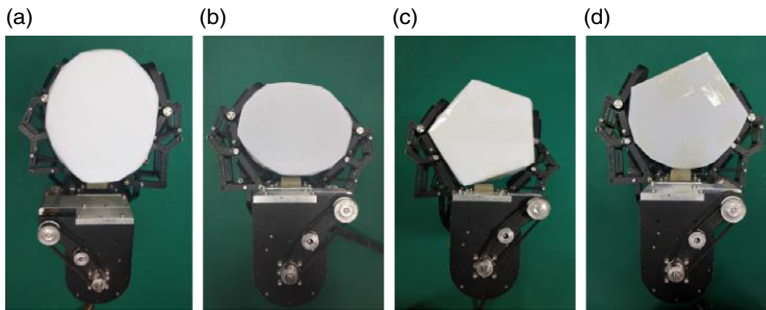
### 5.3. Self-adaptive experiment

Since the holding mechanism has a high adaptability and self-balancing capability of internal forces for holding objects, the designed climbing robot can hold and climb on objects with a wide range size (radius continuously varying from 40 to 100 mm). When holding objects with radius less than 40 mm, the robotic holding mechanism on both sides eventually interferes with the base. When holding objects with radius larger than 100 mm, the robot cannot form a closed grasp, so the stability is greatly reduced. In addition, the designed climbing robot can climb on elliptic(a,b), polygon(c), irregular objects(d) as shown in Fig. 19 and some other irregularly shaped objects with the external diameter between 40 and 100 mm.

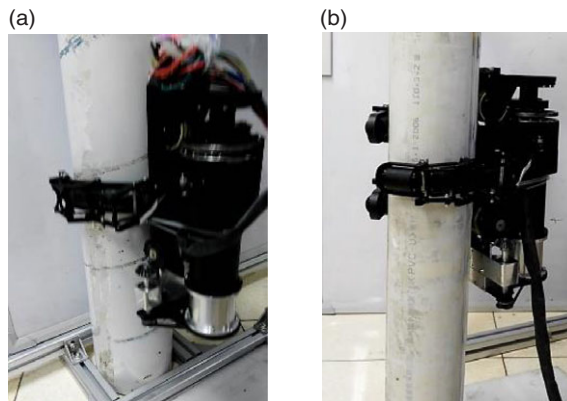
### 5.4. Climbing experiment

Based on the contact force analysis and the designed MRAC controller, Fig. 20 shows the climbing process of the underactuated climbing robot on different diameter cylinders ( $\varphi 90$  mm,  $\varphi 70$  mm). The





**Figure 19.** Robotic climbing adaptability in top view. (a) Elliptic (horizontal). (b) Elliptic (vertical). (c) Polygon. (d) Irregular.



**Figure 20.** Robot on different objects climbing process. (a) Target object of  $\varphi 90$  mm. (b) Target object of  $\varphi 70$  mm.

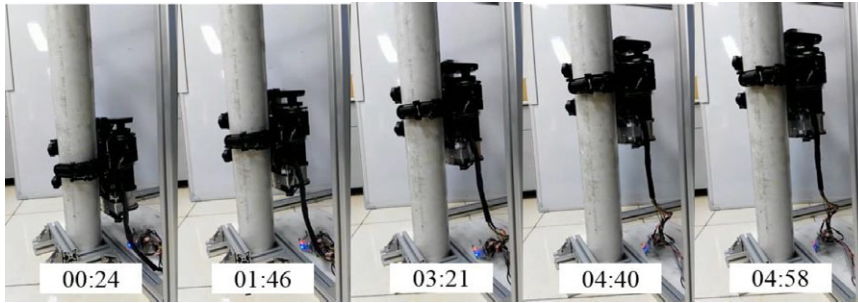
climbing process is stable and firm. Meanwhile, in order to demonstrate high efficiency of the climbing movement, the response time of holding mechanism and the climbing speed of robot have been measured. After repeated experiments, the response time of the holding mechanism is 2.3 s, the climbing speed is 0.194 m/s as shown in Fig. 21, and the maximum moving velocity on the flat surface is 0.407 m/s.

$\Delta Q_i$  is defined as the deviation of rotation angle of each joint when climbing the pole of 90 and 70 mm. As an example, when robot climbs the pole of 90 mm, the joint 1 rotates in an angle of  $Q_{90}$ , and when robot climbs the pole of 70 mm, the joint 1 rotates in an angle of  $Q_{70}$ .  $\Delta Q_1$  is the deviation angle of joint 1 from the situation of climbing the pole of 90 to 70 mm, which is  $\Delta Q = Q_{90} - Q_{70}$ .

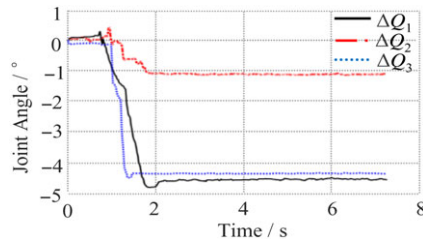
When climbing the pole of 90 and 70 mm, the results of  $\Delta Q_i$  are shown in Fig. 22. Joint 1 ( $\Delta Q_1$ ) is close to both sides of the robot base. It is obvious that the corresponding deviation of rotation angle is  $-4.5^\circ$  when holding the two poles. Joint 2 ( $\Delta Q_2$ ) transmits torque as intermediate to joint 3, and the deviation of rotation angle is  $-1.2^\circ$ , which means that joint 2 changes slightly under different climbing situation. The deviation of rotation angle of joint 3 ( $\Delta Q_3$ ) is  $-4.3^\circ$ , as shown in Fig. 22. The required positive pressure of climbing is provided by joint 3.

### 5.5 Ground crawling experiment

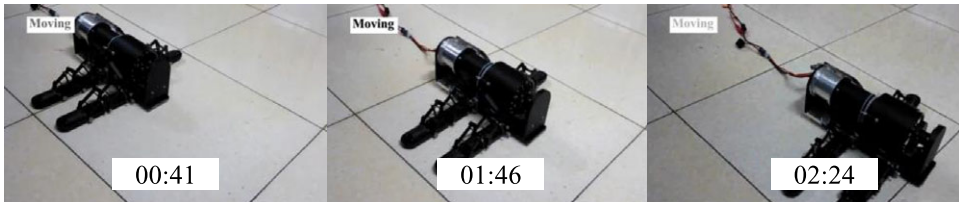
Ground crawling state is the other way of movement of the climbing robot. When crawling on the ground, the holding mechanism is fully unfolded, and the two active wheels of the wheel driving system located under the base provide power, which can make the robot move forward or backward quickly. Due to the deviation of the gravity center caused by the difference in the number of holding mechanisms on



**Figure 21.** Climbing speed experiment. Intercept climbing process from 0.24 to 4.58 s, the climbing height is 0.84 m, and the climbing speed is 0.194 m/s.



**Figure 22.** Deviation of rotation angle of each joint when climbing objects of 90 and 70 mm.



**Figure 23.** Crawling speed experiment. Intercept crawling process from 0.41 to 2.24 s, the climbing length is 0.74 m, and the climbing speed is 0.404 m/s.

both sides, the internal gear and motor system of the drive system are arranged to one side of the single holding mechanism, ensuring that the robot will not roll over.

The crawling speed experiment is designed as shown in Fig. 23. The robot moves on the smooth floor tiles of 800 mm × 800 mm. A video segment of the robot passing by a floor tile is intercepted. After measurement, the robot moves 0.74 m in total, which takes 1.83 s, and the average crawling speed is 0.404 m/s.

## 6. Conclusion

This work proposes an underactuated self-adaptive climbing robot that can hold and climb a variety of poles and move on the ground. The underactuated holding mechanism is designed to realize stable and self-adaptive holding for the target, and three underactuated holding mechanisms are driven by one motor to open and close. The wheel drive system is designed to achieve climbing and ground movement through one motor. Through the parameter design, the dimensions and driving force parameters of the climbing robot are analyzed, which provide a basis for the prototype machining and the motor selection. The MRAC controller is proposed, and the adjustable gain parameters are modified according to the Lyapunov stability theory, which improves the stability and rapid response of the climbing system. Through the model design and the parameter design, the structure and size of the climbing robot are

determined, and the prototype is manufactured. The holding and self-adaptability experiments are carried out to verify the stability and self-adaptability of the holding mechanisms. The climbing experiment and the ground crawling experiment are carried out to verify the robot's movement ability and travel speed.

**Acknowledgements.** This study is supported by National Key R&D Program of China (2018YFB1304600), National Natural Science Foundation of China (51975566, U1908214), CAS Interdisciplinary Innovation Team (JCTD-2018-11), and Liaoning Revitalization Talents Program (XLYC1807090).

**Supplementary Material.** To view supplementary material for this article, please visit <https://doi.org/10.1017/S0263574721001636>.

## References

- [1] D. Schmidt and K. Berns, "Climbing robots for maintenance and inspections of vertical structures—A survey of design aspects and technologies," *Robotics* **61**(12), 1288–1305 (2013).
- [2] H. Zhu, Y. Guan, W. Wu, X. Chen, X. Zhou and H. Zhang, "A binary approximating method for graspable region determination of biped climbing robots," *Adv. Rob.* **28**(21), 1405–1418 (2014).
- [3] E. C. Wu, J. C. Hwang and J. T. Chladek, "Fault-tolerant joint development for the space shuttle remote manipulator system: Analysis and experiment," *IEEE Trans. Robot. Autom.* **9**(5), 675–684 (1993).
- [4] Y. Fukazu, N. Hara, Y. Kanamiya and D. Sato, "Reactionless Resolved Acceleration Control with Vibration Suppression Capability for JEMRMS/SFA," *Proceedings of the 2008 IEEE International Conference on Robotics and Biomimetics, Thailand* (2009) pp. 1359–1364.
- [5] O. Ma, K. Buhariwala, N. Roger, J. MacLean and R. Carr, "MDSF - A generic development and simulation facility for flexible, complex robotic systems," *Robotica* **15**(1), 49–62 (1997).
- [6] R. Boumans and C. Heemskerck, "The european robotic arm for the international space station," *Robot. Auton. Syst.* **23**(1-2), 17–27 (1998).
- [7] Y. Guan, L. Jiang, H. Zhu, X. Zhou and X. Zhang, "Climbot: A Modular Bio-Inspired Biped Climbing Robot," 2011 IEEE/RSJ International Conference on Intelligent Robots and Systems (2011) pp. 1473–1478.
- [8] S. Ueki, H. Kawasaki, Y. Ishigure, K. Koganemaru and Y. Mori, "Development and experimental study of a novel pruning robot," *Artif. Life Rob.* **16**(1), 86–89 (2011).
- [9] S. Yaqub, A. Ali, M. Usman and C. Han, "A spiral curve gait design for a modular snake robot moving on a pipe," *Int. J. Control. Autom.* **17**(10), 2565–2573 (2019).
- [10] K. Jang, Y. K. An, B. Kim and S. Cho, "Automated crack evaluation of a high-rise bridge pier using a ring-type climbing robot," *Comput. Aided Civ. Inf.*, **36**(1), 1–16 (2020).
- [11] A. Baghani, M. N. Ahmadabadi and A. Harati, "Kinematics Modeling of a Wheel-Based Pole Climbing Robot (UT-PCR)," 2005 IEEE International Conference on Robotics and Automation (2005) pp. 2099–2104.
- [12] M. J. Spenko, "Biologically inspired climbing with a hexapedal robot," *J. Field Robot.* **25**(4), 223–242 (2008).
- [13] T. L. Lam and Y. Xu, "Climbing strategy for a flexible tree climbing robot—Treebot," *IEEE Trans. Robot.* **26**(4), 12–23 (2011).
- [14] M. Tavakoli, L. Marques and A. T. de Almeida, "3DClimber: Climbing and manipulation over 3D structures," *Mechatronics* **21**(1), 48–62 (2011).
- [15] S. K. Yun and D. Rus, "Self-Assembly of Modular Manipulators with Active and Passive Modules," IEEE International Conference on Robotics and Automation (2008) pp. 1477–1483.
- [16] V. Boomeri, S. Pourebrahim and H. Tourajzadeh, "Kinematic and Dynamic Modeling of an Infrastructure Hybrid Climbing Robot," IEEE International Conference on Knowledge-Based Engineering and Innovation (2017) pp. 0834–0842.
- [17] A. Peidr , M. Tavakoli, J. M. Mar n and  . Reinoso, "Design of compact switchable magnetic grippers for the HyReCRo structure-climbing robot," *Mechatronics* **59**(1), 199–212 (2019).
- [18] Y. Jiang, "Multimodal pipe-climbing robot with origami clutches and soft modular legs," *Bioinspir. Biomim.* **15**(2), 1–12 (2019).
- [19] S. Chen, H. Zhu, Y. Guan, P. Wu and Z. Hong, "Collision-Free Single-Step Motion Planning of Biped Pole-Climbing Robots in Spatial Trusses," IEEE International Conference on Robotics and Biomimetics (2013) pp. 280–285.
- [20] Y. Liu, H. G. Kim and T. W. Seo, "AnyClimb: A new wall-climbing robotic platform for various curvatures," *IEEE-ASME T. Mech.* **21**(4), 1812–1821 (2016).
- [21] H. G. Kim, M. Sitti and T. W. Seo, "Tail-assisted mobility and stability enhancement in yaw and pitch motions of a water-running robot," *IEEE-ASME T. Mech.* **22**(3), 1207–1217 (2017).
- [22] G. A. Lynch, J. E. Clark and P. C. Lin, "A bioinspired dynamical vertical climbing robot," *Int. J. Robot. Res.* **31**(8), 974–996 (2012).
- [23] S. Kim, M. Spenko, S. Trujillo, B. Heyneman and R. Cutkosky, "Whole Body Adhesion: Hierarchical, Directional and Distributed Control of Adhesive Forces for a Climbing Robot," *IEEE International Conference on Robotics and Automation, Roma* (2007) pp. 1268–1273.

- [24] L. Schiller, A. Seibel and J. Schlattmann, "Toward a gecko-inspired, climbing soft robot," *Front. Neurobot.* 13, Article 106 (2019).
- [25] D. Cruz-Ortiz, M. Ballesteros-Escamilla, I. Chairez and A. Luviano, "Output second-order sliding-mode control for a gecko biomimetic climbing robot," *J. Bionic Eng.* **16**(4), 633–646 (2019).
- [26] Q. Jiang, Z. Wang, J. Zhou, W. Chen and Z. Dai, "Analysis of reaction force and locomotor behavior on geckos in time- and frequency-domain during climbing on vertical substrates," *J. Bionic Eng.* **16**(1), 115–129 (2019).
- [27] L. Wu, G. Carbone and M. Ceccarelli, "Designing an underactuated mechanism for a 1 active DOF finger operation," *Mech. Mach. Theory*, **44**(2), 336–348 (2009).
- [28] M. Mohammed, S. Chua and L. Kwek, "Comprehensive Review on Reaching and Grasping of Objects in Robotics," *Robotica*, **2021**, 1–34 (2021).
- [29] L. Birglen, and C. Gosselin, "Kinetostatic analysis of underactuated fingers," *IEEE T. Robot. Autom.* **20**(2), 211–221 (2004).